

# Cosmic shear and halo abundances: analytical versus numerical results

Katrin Reblinsky<sup>1</sup>, Guido Kruse<sup>1</sup>, Bhuvnesh Jain<sup>2</sup>, and Peter Schneider<sup>1</sup>

<sup>1</sup> Max-Planck Institut für Astrophysik, Postfach 1523, D-85740 Garching, Germany

<sup>2</sup> Johns Hopkins University, Department of Physics, Baltimore, MD 21218, USA

Received ; accepted

**Abstract.** The aperture mass has been shown in a series of recent publications to be a useful quantitative tool for weak lensing studies, ranging from cosmic shear to the detection of a mass-selected sample of dark matter haloes. Quantitative analytical predictions for the aperture mass have been based on a number of simplifying assumptions. In this paper, we test the reliability of these assumptions and the quality of the analytic approximations, using ray-tracing simulations through a cosmological density field generated by very large N-body simulations. We find that those analytic predictions which take into account the non-linear evolution of the matter distribution, such as the dispersion of the aperture mass and the halo abundance, are surprisingly accurately reproduced with our numerical results, whereas the predictions for the skewness, based on quasi-linear theory, are rather imprecise. In particular, we verify numerically that the probability distribution of the aperture mass decreases exponentially for values much larger than the rms. Given the good overall agreement, comparisons between the observed distribution of the aperture mass and the theoretical values provide a powerful tool for testing cosmological models.

**Key words:** cosmology: theory – cosmology: dark matter – cosmology: gravitational lensing – cosmology: large scale structure of the Universe – methods: numerical

## 1. Introduction

The gravitational distortion of light bundles from distant sources in the universe provides a unique means to investigate (the statistical properties of) the intervening mass distribution. Being observable through the image distortion of the distant faint blue galaxy population, this cosmic shear effect offers the opportunity to study statistical properties of the large-scale structure. In contrast to almost all other methods for investigating the large scale structure (LSS) – with CMB being the only

*Send offprint requests to:* Katrin Reblinsky (reblinsk@mpa-garching.mpg.de)

exception – no assumption about the relation between dark and luminous mass is required.

Based on the assumption that the intrinsic orientation of the background galaxies is random, a net alignment in the observed galaxy images can be attributed to the tidal field (shear). Hence, the alignment pattern of the galaxy images directly reflects the properties of the mass distribution. For example, two-point statistical measures of the galaxy ellipticities (understood here and in the following as two-component quantities, with an amplitude and an orientation) can be expressed directly in terms of the power spectrum of the mass distribution, convolved with a filter function (Blandford et al. 1991; Miralda-Escudé 1991; Kaiser 1992; Jain & Seljak 1997; Bernardeau et al. 1997; Schneider et al. 1998, hereafter SvWJK; Kaiser 1998; van Waerbeke et al. 1999; Jain et al. 1999, hereafter JSW; and references therein). The power spectrum completely characterises a Gaussian random density field, and so the two-point statistics, like the two-point correlation function of galaxy ellipticities or the rms shear in an aperture, suffices to extract the statistical information contained in the distorted galaxy images. Whereas the earlier of the aforementioned papers concentrated mainly on predictions for the cosmic shear based on the linear evolution of the cosmic density field, it was pointed out by Jain & Seljak (1997) that even on scales as large as one degree, the non-linear evolution significantly affects the expected amplitude of the cosmic shear.

The non-linear evolution transforms an initially Gaussian field into a non-Gaussian one, and thus the cosmic shear on small angular scales is expected to display significant non-Gaussian features. As pointed out by Bernardeau et al. (1997) and SvWJK, the skewness of the resulting cosmic shear field is a sensitive measure of the density factor  $\Omega_0$ , since in quasi-linear perturbation theory the skewness is independent of the normalisation of the initial power spectrum. In order to define the skewness, mass reconstruction algorithms such as those developed for cluster reconstructions (Kaiser & Squires 1993; Seitz & Schneider 1996; Seitz et al. 1998a; Lombardi & Bertin 1998a,b; and references therein) can be employed

to reconstruct the projected density field. This density field, appropriately spatially filtered, can then be used to calculate the skewness. In contrast to the two-point statistical measures mentioned above, which are defined directly in terms of the observable image ellipticities, this measurement of skewness is more indirect. This causes estimates of the statistical error from the data itself not to be straightforward. On the other hand, the aperture mass  $M_{\text{ap}}$ , introduced as a measure for cosmic shear in SvWJK, is a scalar quantity directly defined in terms of the image ellipticities, and can thus be easily used for defining a skewness, as well as a second order statistics, the rms of  $M_{\text{ap}}(\theta)$ , where  $\theta$  is the angular scale of the circular aperture (definitions are given in Sect. 2 below). In particular, in contrast to the two-point ellipticity correlation function and the rms shear in an aperture, for which the filter with which the power spectrum of the projected density field is measured is broad, the corresponding filter function for the rms of  $M_{\text{ap}}(\theta)$  is very narrow, and can be approximated very accurately by a delta “function”, so that  $M_{\text{ap}}(\theta)$  directly measures the power of the projected density at wavelength  $\ell \approx 4.25/\theta$  (Bartelmann & Schneider 1999). The skewness defined in terms of  $M_{\text{ap}}$  has been considered in SvWJK.

As in the evolution of the three-dimensional density field, where highly non-linear structures like clusters of galaxies form, the projected mass density attains strongly non-Gaussian features, e.g., the projection of collapsed haloes. As a scalar quantity, the aperture mass is ideally suited to probe the full probability distribution of the projected mass density; in particular, values of  $M_{\text{ap}}(\theta)$  far out in the non-Gaussian tail signal the presence of massive dark matter haloes. Therefore, peaks in the distribution of  $M_{\text{ap}}$  can be used to search for such haloes, independent of their luminous properties (Schneider 1996, hereafter S96). Indeed, a first application of  $M_{\text{ap}}$  to large scale structure simulations by Reblinsky & Bartelmann (1999) revealed that the detection of dark matter haloes through the aperture mass is more reliable in terms of completeness and spurious detections and suffers less from projection effects than optically selected cluster samples. Assuming that highly significant peaks are caused by such haloes, one can predict their abundance (i.e., number of peaks above a certain threshold per unit solid angle) by combining the spatial abundance as predicted by Press & Schechter (1974) theory with an assumed density profile, such as the universal dark matter profile found by Navarro et al. (1996, 1997; combined NFW). This idea has been put forward by Kruse & Schneider (1999a; hereafter KS1), who found that, depending on the cosmological model and the redshift distribution of background galaxies, of order 10 such haloes per square degree will be detectable in deep ground-based optical images, with a signal-to-noise ratio larger than 5. Given the rapid evolution of wide-field imaging, a mass-selected sample of dark matter haloes is now well within reach. Indeed, a first example

of a shear-detected mass concentration has recently been found by Erben et al. (1999).

All of these predictions on cosmic shear are made using simplifying assumptions in order to make analytic progress. JSW tested some of these assumptions using ray-tracing simulation through a cosmic density field generated by very large N-body simulations; similar tests have been carried out by van Waerbeke et al. (1999). They found that the major approximations made in these analytic treatments, namely the so-called “Born-approximation” (which projects the density fields along “straight lines”), and the neglect of non-linear terms in the propagation equations, are very well satisfied. In particular, the twist of light bundles, which vanishes identically in the usual analytical treatments, is indeed very small. The predictions on the projected power spectrum using the approximation for the fully non-linear power spectrum of Peacock & Dodds (1996) agree very well with the numerical results, whereas the predictions concerning the skewness are less precise, indicating a breakdown of quasi-linear perturbation theory on small scales.

In this paper, we extend the study of JSW to the particular application of the aperture mass statistics. We use the same simulations as JSW, resulting in a table of shear and projected mass density as a function of angular position. From the shear, we can simulate observations of the aperture mass as a function of position on the “data” field, and investigate its statistical properties. In particular, we calculate the probability distribution of  $M_{\text{ap}}(\theta)$ , which we find to be highly non-Gaussian, and from that we study the dispersion, skewness and kurtosis of the distribution. In agreement with JSW, we find that the dispersion is accurately predicted by analytic theory, whereas the skewness predictions can differ substantially from the numerical results. Of particular interest is the kurtosis, since it enters the determination of the uncertainty of the dispersion measurement due to cosmic variance (SvWJK). We find that the kurtosis is a slowly decreasing function of angular scale  $\theta$ , and attains values of  $\sim 3$  even on scales as large as  $10'$ ; hence, the cosmic variance will be the major source of statistical error in the measurement of the power spectrum of the projected density field from  $M_{\text{ap}}$ . The analytic predictions on the abundance of significant peaks of  $M_{\text{ap}}$ , and thus presumably of dark matter haloes, turns out to be remarkably precise, given the strong assumptions made. We confirm the high number density of haloes detectable with this method. The shape of the probability distribution of  $M_{\text{ap}}$  in the highly non-Gaussian tail, predicted by Kruse & Schneider (1999b; hereafter KS2), can also be confirmed to be well approximated by an exponential function.

## 2. The aperture mass measure $M_{\text{ap}}$

In this section, we briefly summarise the properties of the aperture mass, i.e., its definition, its relation to the shear, and its signal-to-noise ratio. For more details, the reader is referred to S96 and SvWJK.

### 2.1. $M_{\text{ap}}$ statistics

We define the spatially filtered mass inside a circular aperture of angular radius  $\theta$  around the point  $\zeta$  by

$$M_{\text{ap}}(\zeta) := \int d^2\vartheta \kappa(\vartheta) U(|\vartheta - \zeta|), \quad (1)$$

where the continuous weight function  $U(\vartheta)$  vanishes for  $\vartheta > \theta$ . If  $U(\vartheta)$  is a compensated filter function,

$$\int_0^\theta d\vartheta \vartheta U(\vartheta) = 0, \quad (2)$$

one can express  $M_{\text{ap}}$  in terms of the tangential shear  $\gamma_t(\xi; \zeta)$  at position  $\xi + \zeta$  relative to  $\zeta$  as

$$M_{\text{ap}}(\zeta) = \int d^2\xi \gamma_t(\xi; \zeta) Q(|\xi|), \quad (3)$$

(Fahlmann et al. 1994; S96), where

$$\gamma_t(\xi; \zeta) = -\text{Re}(\gamma(\xi + \zeta) e^{-2i\phi}), \quad (4)$$

and  $\phi$  is the polar angle of  $\xi$ . The function  $Q$  is related to  $U$  by

$$Q(\vartheta) = \frac{2}{\vartheta^2} \int_0^\vartheta d\vartheta' \vartheta' U(\vartheta') - U(\vartheta). \quad (5)$$

We use the filter function for  $l = 1$  from the family given in SvWJK: writing  $U(\vartheta) = u(\vartheta/\theta)/\vartheta^2$ , and  $Q(\vartheta) = q(\vartheta/\theta)/\vartheta^2$ , we take

$$u(x) = \frac{9}{\pi} (1 - x^2) \left( \frac{1}{3} - x^2 \right), \quad (6)$$

and

$$q(x) = \frac{6}{\pi} x^2 (1 - x^2), \quad (7)$$

with  $u(x) = 0 = q(x)$  for  $x > 1$ .

### 2.2. Signal-to-noise ratio

An estimate of the shear field  $\gamma$ , and thus of the aperture mass  $M_{\text{ap}}(\vartheta)$  through Eq. (3), is provided by the distortions of images of faint background galaxies. The complex ellipticity of galaxy images is defined in terms of second moments of the surface-brightness tensor (e.g., Tyson et al. 1990; Kaiser & Squires 1993). Specifically, we use here the ellipticity parameter  $\epsilon$  (Schneider 1995; Seitz & Schneider 1997), which is defined such that for sources with elliptical isophotes of axis ratio  $r \leq 1$ , the modulus of the source ellipticities is given as  $|\epsilon^{(s)}| = (1 - r)/(1 + r)$ ,

and the phase of the  $\epsilon^{(s)}$  is twice the position angle of the major axis.

The complex image ellipticity  $\epsilon$  can then be calculated in terms of the source ellipticity  $\epsilon^{(s)}$  and the reduced shear  $g \equiv \gamma(1 - \kappa)^{-1}$  by the transformation (Seitz & Schneider 1997)

$$\epsilon = \frac{\epsilon^{(s)} + g}{1 + g^* \epsilon^{(s)}}. \quad (8)$$

This relation is valid only for noncritical clusters. For critical clusters, it has to be replaced by a different transformation. However, as we are mainly interested in the weak lensing regime, the above relation is sufficient here.

It has been demonstrated (Schramm & Kayser 1995; Seitz & Schneider 1997) that the ellipticity  $\epsilon$  of a galaxy image is an unbiased estimate of the local reduced shear, provided that the intrinsic orientations of the sources are random. In the case of weak lensing,  $\kappa \ll 1$ , one then has

$$\langle \epsilon \rangle = g \approx \gamma \quad (9)$$

by averaging (8) with the probability distribution of the source ellipticities.

As for the tangential shear component  $\gamma_t$  occurring in (4), a similar quantity for the image ellipticities can be defined. Consider a galaxy image  $i$  at a position  $\vartheta_i + \zeta$  relative to the point  $\zeta$  with a complex image ellipticity  $\epsilon_i$ . In analogy to (4) the tangential ellipticity  $\epsilon_{ti}(\vartheta_i; \zeta)$  of this galaxy is then given by

$$\epsilon_{ti}(\vartheta_i; \zeta) = -\text{Re}(\epsilon_i(\vartheta_i + \zeta) e^{-2i\phi_i}), \quad (10)$$

where  $\phi_i$  is the polar angle of  $\vartheta_i$ .

We can now estimate the integral (3) by a discrete sum over galaxy images,

$$M_{\text{ap}}(\zeta) = \frac{1}{n} \sum_i \epsilon_{ti}(\vartheta_i; \zeta) Q(|\vartheta_i|), \quad (11)$$

where  $n$  is the number density of galaxy images. The discrete dispersion  $\sigma_d$  of the aperture mass  $M_{\text{ap}}(\zeta)$  is found by squaring (11) and taking the expectation value in the absence of lensing, which leads to

$$\sigma_d^2 = \frac{\sigma_\epsilon^2}{2n^2} \sum_i Q^2(|\vartheta_i|), \quad (12)$$

where  $\sigma_\epsilon^2 = \langle |\epsilon^{(s)}|^2 \rangle$ . Performing an ensemble average of Eq. (12) leads to the continuous dispersion  $\sigma_c$

$$\sigma_c^2(\theta) = \frac{\pi \sigma_\epsilon^2}{n} \int_0^\theta d\vartheta \vartheta Q^2(\vartheta). \quad (13)$$

Finally, the *signal-to-noise* ratio  $S$  at position  $\zeta$  is

$$S(\zeta) \equiv \frac{M_{\text{ap}}(\zeta)}{\sigma_d} = \frac{\sqrt{2}}{\sigma_\epsilon} \frac{\sum_i \epsilon_{ti}(\vartheta_i; \zeta) Q(|\vartheta_i|)}{[\sum_i Q^2(|\vartheta_i|)]^{1/2}}. \quad (14)$$

In the simulations, we draw the source ellipticities from a Gaussian probability distribution,

$$p_s(|\epsilon^{(s)}|) = \frac{1}{\pi\sigma_\epsilon^2 [1 - \exp(-\sigma_\epsilon^{-2})]} \exp\left(-\frac{|\epsilon^{(s)}|^2}{\sigma_\epsilon^2}\right), \quad (15)$$

where the width of the distribution is chosen as  $\sigma_\epsilon = 0.2$ . Throughout this paper, we assume that the number density of the background sources is  $n = 30 \text{ arcmin}^{-2}$ .

### 2.3. Analytical work done with $M_{\text{ap}}$

The aperture mass has been considered in the framework of blank field surveys in a variety of earlier publications. Introduced as a convenient statistics for cosmic shear, SvWJK have calculated the rms of  $M_{\text{ap}}$  as a function of angular scale, using the Peacock & Dodds (1996) approximation for the non-linear evolution of the power spectrum of density fluctuations. Like other two-point statistics, the dispersion of  $M_{\text{ap}}$  is an integral over the power spectrum of the projected mass distribution, weighted by a filter function. The filter function corresponding to  $\langle M_{\text{ap}}^2 \rangle$  is very narrow and can be well approximated by a delta function (Bartelmann & Schneider 1999). Hence,  $\langle M_{\text{ap}}^2(\theta) \rangle$  reproduces the shape of the projected power spectrum and, depending on the cosmological model and the redshift distribution of the sources, it reveals a broad peak at  $\theta \sim 1'$ . One convenient property of the aperture mass is that the correlation function of  $M_{\text{ap}}$  of two apertures spatially separated by  $\Delta\theta$  quickly decreases and already achieves values of  $10^{-2}$  for  $\Delta\theta \sim 2\theta$ . This means that measurements of  $M_{\text{ap}}$  from a large consecutive area can be considered independent if the apertures are densely laid out on this data field; this is in contrast to the rms shear in apertures which is strongly correlated, and thus must be obtained from widely separated regions on the sky.

Being a scalar quantity,  $M_{\text{ap}}$  can also be used for higher-order statistical measures of the cosmic shear. SvWJK calculated the skewness of  $M_{\text{ap}}$ , using Eulerian perturbation theory for the evolution of the three-dimensional density contrast  $\delta$ . In agreement with Bernardeau et al. (1997) they found that the skewness is a sensitive function of the cosmic density factor  $\Omega_0$ , and is in this approximation independent of the normalisation of the power spectrum.

A measurement of the dispersion of  $M_{\text{ap}}$  is affected by two main sources of statistical error: the intrinsic ellipticity distribution of the source galaxies, and cosmic variance. To estimate the latter, one needs to know the kurtosis of  $M_{\text{ap}}$  which cannot easily be determined analytically.

Values of  $M_{\text{ap}}$  much larger than its rms probe the highly non-Gaussian regime of the projected density field. From its definition, one sees that large values of  $M_{\text{ap}}$  are expected if the aperture is centred on a density peak with a size comparable to the filter scale

$\theta$ . Therefore, the aperture map can be used to search for such density peaks, presumably collapsed dark matter haloes, in blank field imaging surveys. In this way it is possible to obtain a mass-selected sample of such haloes (S96). Simple analytical arguments in S96 suggest that dark matter haloes with an approximately isothermal profile are detectable with a signal-to-noise ratio larger than 5 if their velocity dispersion exceeds  $\sim 600 \text{ km/s}$ , assuming a number density of background sources of  $n \sim 30 \text{ arcmin}^{-2}$ . Indeed, this theoretical expectation was verified in the lensing investigation of the cluster MS1512+36 (Seitz et al. 1998b). This cluster has a velocity dispersion of about  $\sim 600 \text{ km/s}$ , as obtained from strong lensing modelling and from spectroscopy of cluster members, and is detected in the weak lensing analysis with very high statistical significance.

Assuming that the high signal-to-noise peaks of  $M_{\text{ap}}$  are due to collapsed dark matter haloes, one can attempt to estimate the abundance of such peaks using analytic theory. KS1 have calculated the number density of haloes with aperture mass larger than  $M_{\text{ap}}$ ,  $N(> M_{\text{ap}}, \theta)$ , assuming (1) that dark matter haloes are distributed according to Press & Schechter (1974) theory which yields the number density of collapsed haloes as a function of halo mass and redshift, and (2) that the azimuthally-averaged projected density profiles of these haloes can be described by the projection of the universal halo density profile found in numerical simulations by NFW. Depending on the cosmological model and on the redshift distribution of the faint galaxies, the number density of peaks of  $M_{\text{ap}}$  with a signal-to-noise ratio larger than 5 was estimated to be  $\gtrsim 10$  per square degree, and the redshift distribution of these haloes is strongly dependent on the behaviour of the linear growth factor for density perturbations, and thus on  $\Omega_0$ . This abundance is encouraging, since it allows one to obtain samples of haloes selected by their mass properties alone (for a first example, see Erben et al. 1999).

Using the same model, KS2 have calculated the probability distribution of  $M_{\text{ap}}$  for values of  $M_{\text{ap}}$  much larger than its rms, assuming that this non-Gaussian tail of the probability distribution is dominated by dark matter haloes. They found that the distribution is very well described by an exponential; i.e., the tail is much broader than for a Gaussian.

All these analytic predictions are based on a number of approximations and simplifying assumptions. In Sect. 4 below we shall compare these analytic results with those found in ray-tracing simulations through a cosmological mass distribution obtained from very large N-body calculations, as described in the next section.

### 3. Generation of shear maps with ray-tracing simulations

Simulated shear maps due to weak lensing by large-scale structure are made by performing ray tracing simulations through the dark matter distribution produced by N-body simulations (JSW). The N-body simulations used are a set of adaptive particle-particle/particle-mesh (AP<sup>3</sup>M) simulations. The long-range component of the gravitational force is computed by solving Poisson's equation on a grid. The grid calculation is supplemented with a short range correction computed either by a direct sum over neighbouring particles, or, in highly clustered regions, by combining a calculation on a localised refinement mesh with a direct sum over a smaller number of much closer neighbours. The parameters used by the N-body simulations are given in Table 1.

The simulations were run with a parallel adaptive AP<sup>3</sup>M code (Couchman et al. 1995; Pearce & Couchman 1997) kindly made available by the Virgo Supercomputing Consortium (e.g. Jenkins et al. 1998). They followed  $256^3$  particles using a force law with softening length  $l_{\text{soft}} \simeq 30 h^{-1}\text{kpc}$  at  $z = 0$  (the force is  $\sim 1/2$  its  $1/r^2$  value at one softening length and is almost exactly Newtonian beyond two softening lengths).  $l_{\text{soft}}$  was kept constant in physical coordinates over the redshift range of interest to us here. The simulations were carried out using 128 or 256 processors on CRAY T3D machines at the Edinburgh Parallel Computer Centre and at the Garching Computer Centre of the Max-Planck Society. These simulations have previously been used for studies of strong lensing by Bartelmann et al. (1998), for studies of dark matter clustering by Jenkins et al. (1998), and for studies of the relation between galaxy formation and galaxy clustering by Kauffmann et al. (1999a,b), and Diaferio et al. (1999).

The ray tracing simulations of weak lensing from which we use the convergence and shear maps were computed by JSW. They used a multiple lens-plane calculation that implements the discrete recursion relations for the position of a given photon and for the Jacobian matrix of the lens mapping at this position (Schneider & Weiss 1988; Schneider et al. 1992; see Seitz et al. 1994 for a thorough justification for this approach). Aside from the distance factors, the main input into the recursion relations is the shear matrix at each lens plane. The ray tracing algorithm consists of three parts: constructing the dark matter lens planes, computing the shear matrix on each plane, and using these to evolve the photon trajectory from the observer to the source. The details involved at each step are as follows:

1. The dark matter distribution between source and observer is projected onto 20 – 30 equally spaced (in comoving distance) lens planes. The particle positions on each plane are interpolated onto a grid of size  $2048^2$ . Since the three-dimensional mass distribution is taken

from a single realisation of the evolution of the LSS, the projected mass distributions of consecutive lens planes are correlated. In order to decorrelate them, the projection is carried out along a randomly chosen one of the three coordinate axes; in addition, the origin of the coordinate system in each lens plane is translated by a random vector and the lens plane is rotated by a random angle. In this way, the projected mass distributions of consecutive lens planes are as independent as possible, given the restriction of only a single realisation of the 3-d matter distribution.

2. On each plane, the shear matrix is computed on a grid by Fourier transforming the projected density and using its Fourier space relation to the shear. The inverse Fourier transform is then used to return to real space.

3. The photons are started on a regular grid on the first lens plane. Perturbations along the line of sight distort this grid and are computed using the relation between deflection angle and projected density. Once we have the photon positions, we interpolate the shear matrix onto them and solve the recursion relations for the Jacobian of the mapping from the  $n$ -th lens plane to the first plane.

4. Solving the recursion relations up to the source plane yields the Jacobian matrix at these positions. Note that the ray tracing is done backwards from the observer to the source, thus ensuring that all the photons reach the observer. The first lens plane is the image plane and has the unperturbed photon positions. All sources are assumed to be at a redshift of  $z_s = 1$ .

There are two kinds of resolution limitations in the ray-tracing simulations. The first reflects the finite size and resolution of our N-body simulations, the second the use of finite grids when computing deflection angles and shear tensors on the lens planes. At the peak redshift of the lensing contribution, both effects give a small scale resolution of order  $0.2'$ . However, since the lens efficiency is not very sharply peaked, effects at other redshifts also enter. Thus depending on the statistical measure being used, the small scale resolution lies in the range  $\sim 0.2' - 0.4'$ .

On large scales the finite box-size of the N-body simulations sets the upper limit on the angular scales available. The angular size of our simulation box at  $z = 1$  is about  $3^\circ$ . Thus on scales comparable to  $1^\circ$ , only a few sample regions are available, leading to large fluctuations across different realisations. We therefore restrict our considerations to apertures with radius  $\theta \leq 10'$  using one realisation for every cosmological model. For the  $\tau$ -CDM model, we use ten different realisations of the ray tracing simulations (i.e., they differ in the direction of projections, the translation and rotation of the projected matter distribution in the individual lens planes) to estimate the cosmic variance.

**Table 1.** Parameters of the N-body simulations.

Simulation	SCDM	$\tau$ CDM	$\Lambda$ CDM	OCDM
$N_{\text{par}}$	$256^3$	$256^3$	$256^3$	$256^3$
$l_{\text{soft}}[h^{-1} \text{ kpc}]$	36	36	30	30
$\Gamma$	0.5	0.21	0.21	0.21
$L_{\text{box}}[h^{-1} \text{ Mpc}]$	85	85	141	141
$\Omega_0$	1.0	1.0	0.3	0.3
$\Lambda_0$	0.0	0.0	0.7	0.0
$H_0$ [km/s/Mpc]	50	50	70	70
$\sigma_8$	0.6	0.6	0.9	0.85
$m_{\text{p}}10^{10}h^{-1}M_{\odot}$	1.0	1.0	1.4	1.4
field size [ $^{\circ}$ ]	2.7	2.7	3.4	3.9

#### 4. Application of $M_{\text{ap}}$ to simulated shear maps

For each of the shear maps generated as described in the last section, we create a 2-dim. “ $M_{\text{ap}}$  map” by simulating “observations” of  $M_{\text{ap}}$  as a function of position on the 2-dim. shear maps. The probability distribution function of  $M_{\text{ap}}$  (PDF) and some of its moments are then calculated for every  $M_{\text{ap}}$  map and compared to the analytical model.

It is most instructive to consider two different sets of simulated maps: in the first, we neglect noise from the intrinsic ellipticity distribution of the background sources and compute  $M_{\text{ap}}$  directly from the shear values on the grid according to Eq. (3). We do this either in the limit of weak lensing, i.e. we use (3) directly, or we replace  $\gamma_t$  in (3) by the reduced shear  $g_t$ , which is the quantity estimated from the observable galaxy ellipticities.

In the second set of simulations we introduce ellipticities of background galaxies according to the distribution function (15). The ellipticities add noise to  $M_{\text{ap}}$ .

The noise-free results are the ones best compared to the analytic results, whereas the ones accounting for intrinsic ellipticities yield a more realistic description of the observational situation. In the following the term “without noise” will refer to the first set of  $M_{\text{ap}}$  simulations, while the term “with noise” will be used for the second one.

As an illustrative example, the 2-dimensional distribution of  $M_{\text{ap}}$  for a standard CDM (SCDM) and an open model (OCDM) is shown in Fig. 1. In both cases high peaks in these maps correspond to haloes in the intervening matter distribution. It is possible to construct a shear-limited sample of haloes from these maps and to determine their abundance.

Comparing the two model universes, we see that the  $M_{\text{ap}}$  maps reflect the different growth of structure in different cosmologies. The  $M_{\text{ap}}$  map of the OCDM model is dominated by many isolated peaks which correspond to already collapsed dark matter haloes. The level of

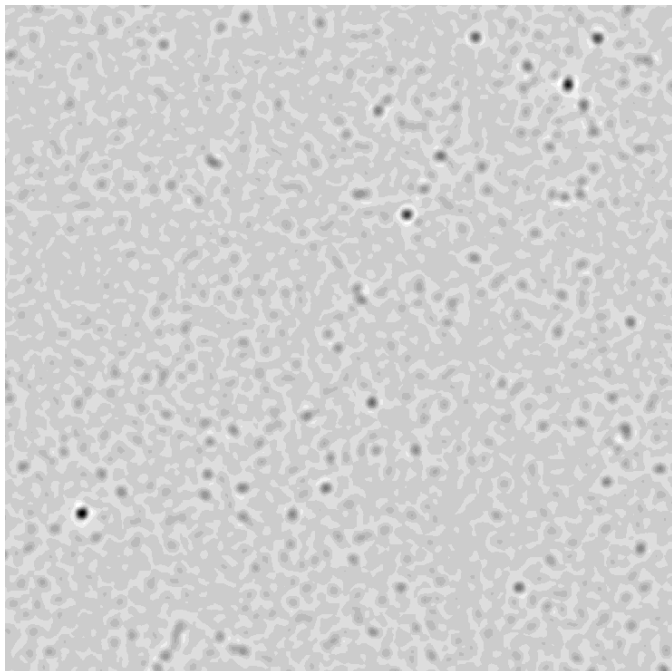
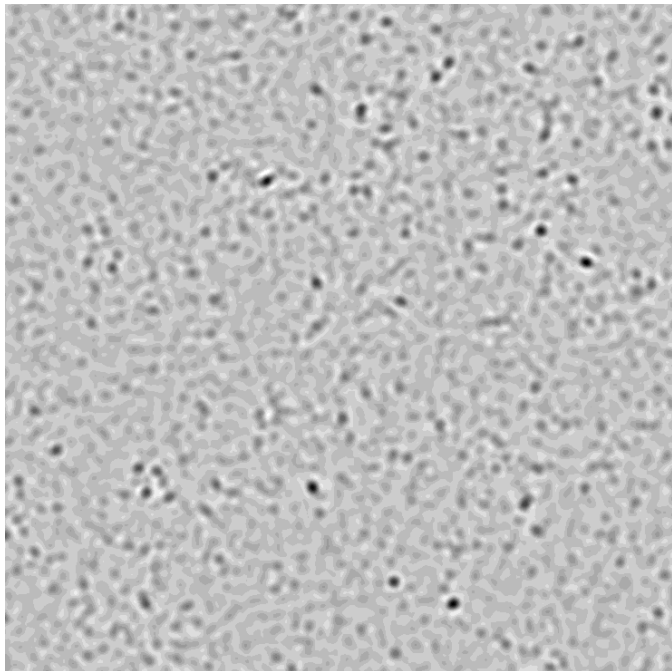


**Fig. 1.** The 2-dimensional distribution of  $M_{\text{ap}}$  for a standard CDM (SCDM, upper panel) and an open model (OCDM,  $\Omega_{\text{m}} = 0.3$ , lower panel), with parameters given in Table 1. The field size in both panels is  $2^{\circ}$ .

background noise coming from matter not yet collapsed is considerably smaller than for the SCDM model in which the structure forms later. The peaks in the SCDM model are less pronounced and isolated than in the open model.

#### 4.1. The PDF of $M_{\text{ap}}$ and its moments

Once we have computed the 2-dimensional distribution of  $M_{\text{ap}}$ , it is straightforward to determine the one-point probability distribution function (PDF) of  $M_{\text{ap}}$  and its moments. The PDF contains the cosmological information. The lower order moments like rms value and skewness can be derived analytically under simplifying assumptions, but the PDF itself cannot be calculated. Therefore, ray tracing simulations provide the only tool for testing the precision of the analytical calculations.

The qualitative features of the PDF for different filter scales  $\theta$  and for the four different cosmologies (Table 1) can be studied in Fig. 2. The first point to note is that the non-Gaussian features, namely the tail of the PDF at high  $M_{\text{ap}}$  values, are less pronounced for larger filter scales. This is due to the fact that the smaller filter scales are more sensitive to the already collapsed, non-linear objects. The second feature to note is the exponential decrease of the tail of  $M_{\text{ap}}$  which was already obtained semi-analytically in KS2. We shall discuss this feature in more detail later in this section.

We now turn to the rms value  $\langle M_{\text{ap}}^2 \rangle^{1/2}$  of  $M_{\text{ap}}$ . Fig. 3 compares the analytical rms value of  $M_{\text{ap}}$  calculated using the nonlinear power spectrum of Peacock & Dodds (1996) to the rms values computed from the PDFs without noise for  $\gamma_t$  (left panel) and  $g_t$  (right panel). The comparison of the latter shows that the difference between shear and reduced shear is negligible even on filter scales as small as  $\theta \sim 2$  arcmin corresponding to the highly nonlinear regime of the mass distribution.

In the left panel of Fig. 3, there is an excellent agreement between the analytic predictions and the rms values computed from simulations for the SCDM model. There is also good agreement for the  $\Lambda$ CDM and OCDM models, especially for the larger apertures. The notable exception is the  $\tau$ CDM model, for which the simulations for small filters deviate by a larger factor from the theoretical predictions.

When interpreting this difference between analytical calculation and simulation in the  $\tau$ CDM model, one has to keep in mind that the numerical results of Fig. 3 are based on a single realisation. As the cosmic variance is relatively large, it is possible that the large deviation is due to the special choice of the realisation. This interpretation is supported by the fact that the mean for the 10 realisations is considerable lower than for the single realisation plotted. Furthermore, the field sizes of the simulated fields used are too small to represent a characteristic region of the universe.

The next higher moment of the PDF is the skewness, which is defined as

$$S_3(\theta) := \frac{\langle M_{\text{ap}}^3 \rangle}{\langle M_{\text{ap}}^2 \rangle^2}, \quad (16)$$

for which we can perform a similar analysis as for the rms value of  $M_{\text{ap}}$ . As pointed out by Bernardeau et

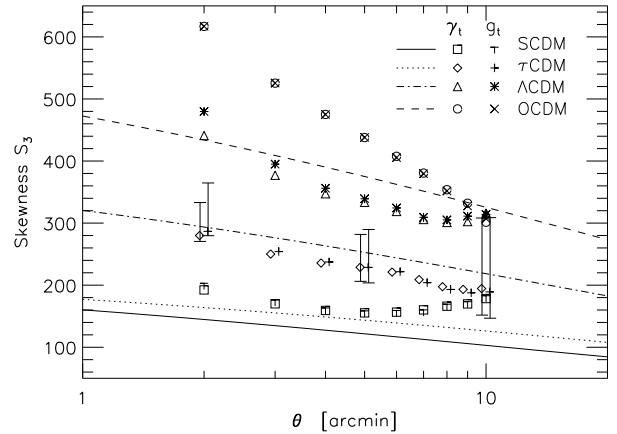


**Fig. 4.** The skewness  $S_3$  of the PDF of  $M_{\text{ap}}$  as defined in (16) as a function of filter scale  $\theta$  for the same cosmological models as in Fig. 2. The analytical skewness (lines) from quasi-linear theory is compared to the skewness obtained from the PDF for both, the tangential shear  $\gamma_t$  and the reduced shear  $g_t$ . Errors on the  $\tau$ CDM model like in Fig. 3.

al. (1997), van Waerbeke et al. (1999), and JSW, the skewness defined in analogy to (16) using a top-hat filter is a very sensitive probe of the cosmic density parameter  $\Omega_0$ .

The dependence of the skewness on filter scale  $\theta$  is displayed in Fig. 4. Again, we compare the skewness computed from the PDF obtained from the ray tracing simulations without noise, both using  $\gamma_t$  and  $g_t$ , to the skewness of  $M_{\text{ap}}$  obtained using quasi-linear theory (SvWJK). The error bars on the skewness for the  $\tau$ CDM model for 2, 5, and 10 arcmin are derived from the 10 different realisations and are centred on their arithmetic mean.

Again, the differences between the skewness obtained from simulations with  $\gamma_t$  and  $g_t$  are small, though slightly larger than for the dispersion, owing to the larger contribution from high- $\kappa$  regions to the skewness. This difference, which is of order a few percent at most, has been predicted to be small in the Appendix of SvWJK.

When comparing the skewness as determined from second-order perturbation theory for the density evolution to that obtained from simulations (either computed with  $\gamma_t$  or  $g_t$ ) we see that the former underpredicts the skewness by factors of up to 2. This failure of quasi-linear theory for the prediction of higher-order moments has been demonstrated previously (Jain & Seljak 1997; Gaztanaga & Bernardeau 1998). As we only determine the skewness on scales below 10 arcmin, we are in a regime where the density contrast is non-linear already. The skewness as calculated by Hui (1999) using the so-called hyper-extended perturbation theory (Scoccimarro & Frieman 1999) may provide a more accurate analytical

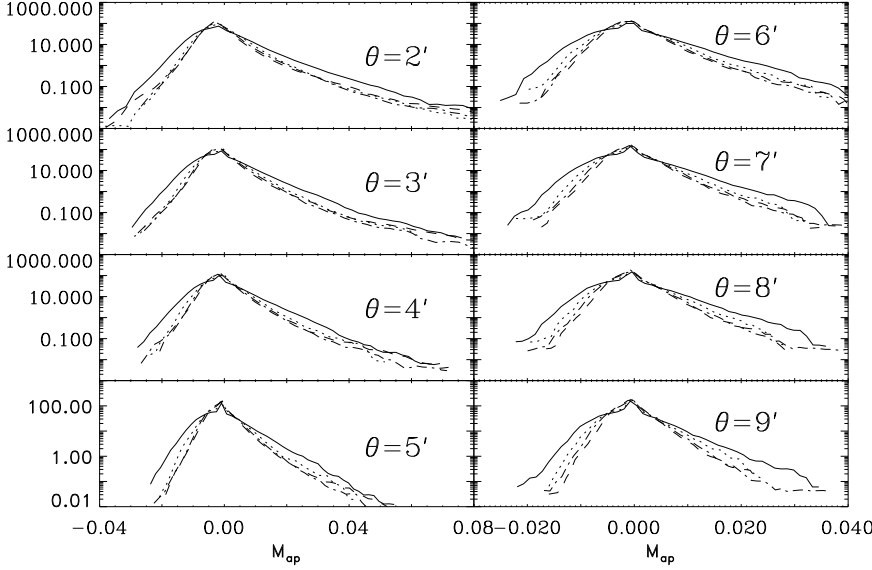


**Fig. 2.** The normalised PDF of  $M_{\text{ap}}$  for different filter scales  $\theta$  and cosmologies: SCDM (solid line),  $\tau$ CDM (dotted line), OCDM (dashed line) and  $\Lambda$ CDM (dashed-dotted line). The histograms are obtained from  $M_{\text{ap}}$  maps without noise. Note the different scales on the horizontal axis.

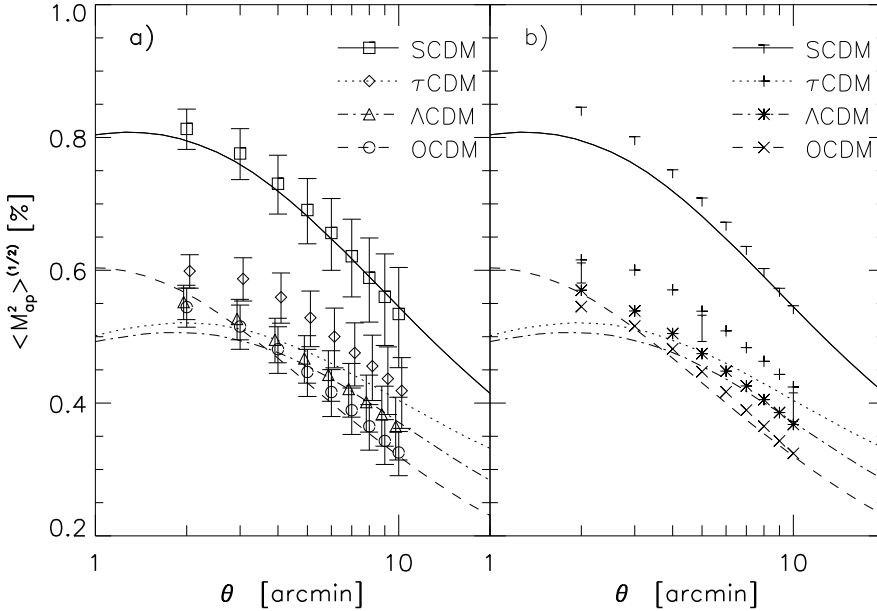


**Fig. 3.** The rms value of  $M_{\text{ap}}$  computed with the filter (6) versus filter scale  $\theta$  for different cosmologies. Lines refer to analytic values of  $\langle M_{\text{ap}}^2 \rangle^{1/2}$  from SvWJK, while symbols refer to rms values obtained from simulations without noise, using  $\gamma_t$  (left panel) and  $g_t$  (right panel). The error bars in the left panel are determined from (20) and (19). The symbols for OCDM and  $\tau$ CDM are slightly offset on the  $\theta$ -axis for better display. The error bars in the right panel show the standard errors from 10 realisations of the  $\tau$ CDM model for 2, 5, and 10 arcmin. They are centred on the arithmetic mean (*not* on the realisation plotted).

prediction of  $S_3$  than that from second-order perturbation theory.

Another point to note is the increase of the skewness towards smaller filter scales. Generally speaking, such a behaviour is expected, as the non-linear structure growth becomes more and more important for small filter scales. This increase is described insufficiently by quasi-linear theory: for the two EdS universes and even for the  $\Lambda$  model on large filter scales above 5 arcmin, this increase (not the absolute value!) is predicted satisfactorily, but the slope for the open model is larger than analytic values on all scales displayed. This discrepancy between

fully non-linear simulations and quasi-linear theory can be attributed to the fact that the open model is much more dominated by already collapsed, non-linear objects than all other models.

The highest moment we consider explicitly is the kurtosis  $S_4$

$$S_4(\Theta) := \frac{\langle M_{\text{ap}}^4 \rangle}{\langle M_{\text{ap}}^2 \rangle^2} - 3. \quad (17)$$

The kurtosis is not only important by itself, but also for the determination of the error of the rms value of  $M_{\text{ap}}$ , as will be discussed. As for the skewness, the



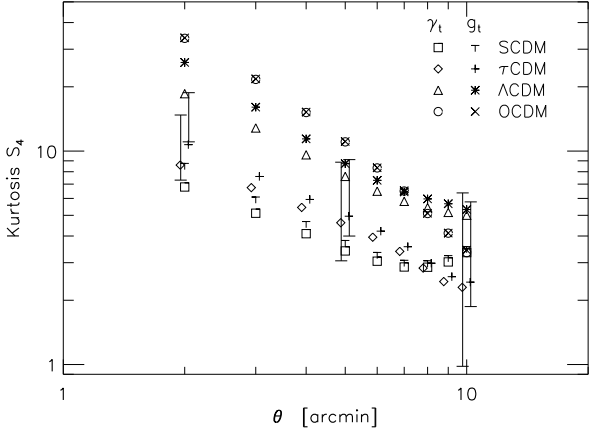


**Fig. 5.** The kurtosis  $S_4$  of the PDF of  $M_{\text{ap}}$  [Eq. (17)] as a function of filter scale  $\theta$ , for the four cosmological models. The kurtosis is derived from the PDF for both, the tangential shear  $\gamma_t$  and the reduced shear  $g_t$ . Errors on the  $\tau$ CDM model are like in Fig. 3. No analytic estimate of the kurtosis has been calculated.

kurtosis for the noise-free simulations for both  $\gamma_t$  and  $g_t$  is plotted, and the scatter for  $\tau$ CDM is determined from the 10 realisations. No analytic result for  $S_4$  is available; however, using third-order perturbation theory, Bernardeau (1998) has calculated the kurtosis for a top-hat filter.

We clearly see that the difference between  $\gamma_t$  and  $g_t$  becomes important for the kurtosis, at least for the smaller filter scales, since it is even more dominated by the non-Gaussian tail of the PDF than the skewness. The large error bars on the kurtosis are mainly due to large cosmic variance in combination with the small fields used; thus, the current simulations are unable to provide an accurate determination of  $S_4$ .

We now turn to the error bars on the rms values of  $M_{\text{ap}}$  in Fig. 3. In the right panel, they were estimated as the standard deviation from 10 different realisations for the  $\tau$ CDM model. The error bars in the left panel were calculated as follows:

As shown in SvWJK, an unbiased estimator of  $\langle M_{\text{ap}}^2 \rangle$  from a single aperture is given by

$$M = \frac{(\pi\theta^2)^2}{N(N-1)} \sum_{i,j \neq i}^N Q_i Q_j \epsilon_{ti} \epsilon_{tj}, \quad (18)$$

where  $N$  is the number of galaxies in the aperture, and  $Q_i$  is the value of the weight function  $Q$  for the  $i$ -th galaxy. The dispersion of this estimator is

$$\sigma^2(M) \approx S_4 \langle M_{\text{ap}}^2 \rangle^2 + \left( \frac{6\sigma_\epsilon^2}{5\sqrt{2}N} + \sqrt{2} \langle M_{\text{ap}}^2 \rangle \right)^2, \quad (19)$$

where the two terms in parenthesis correspond to the noise from the intrinsic ellipticity distribution, and the

Gaussian cosmic variance, respectively, whereas the term involving  $S_4$  is the excess cosmic variance due to non-Gaussianity. For a collection of  $N_f$  independent apertures, all containing the same number of galaxy images, an unbiased estimator for  $\langle M_{\text{ap}}^2 \rangle$  is the mean  $\mathcal{M}$  of  $M$  over these apertures, and the dispersion is

$$\sigma(\mathcal{M}) = \frac{\sigma(M)}{\sqrt{N_f}}. \quad (20)$$

Note that this result does not assume that the density field is Gaussian. If one had a collection of  $N_f$  fields widely separated on the sky, they would be statistically independent, so that  $N_f = N$ . In the opposite situation where a consecutive area on the sky is available, one can lay down apertures on that field, but they will not be statistically independent. However, as was shown in SvWJK, the  $M_{\text{ap}}$  values of two apertures which touch each other (i.e., with separation twice their radii), are almost uncorrelated. Whereas the fact that the two aperture masses in these two apertures are uncorrelated does *not* imply that they are *independent* (which would mean that the joint probability distribution for the values of  $M_{\text{ap}}$  would factorize) – as would be the case for Gaussian fields – we assume the statistical independence for estimating the effective number of fields  $N_f$  entering (20). Thus, the error bars in the left panel of Fig. 3 are obtained from (20), assuming that the number of independent apertures is  $N_f = [\Theta/(2\theta)]^2$ , where  $\Theta$  is the side length of the simulated shear field.

In contrast, the error bars plotted in the right panel of Fig. 3 for the  $\tau$ CDM model at the three different filter scales  $\theta = 2, 5, 10$  arcmin are based on 10 different realisations of the ray-tracing simulations and allow one to obtain a rough estimate for the error from cosmic variance. Notice that the error bars are centred on the arithmetic mean of the 10 realisations and *not* on the plotted results from a single realisation.

Comparing the size of the error bars in both panels, we see that both methods give errors of the same order of magnitude even though the errors estimated from the 10 realisations are smaller than the errors from the estimator of  $\langle M_{\text{ap}} \rangle$ . There are two possible reasons for this: first, the effective number of independent apertures is probably larger than our estimate given above, so that the error bars on the left panel in Fig. 3 most likely overestimate the true error. Second, in the calculation of the error bars in the right panel, it was assumed that the 10 realisations are independent; but as argued in Sect. 3 it is possible that the realisations are not completely independent. This would lead to an underestimation of the cosmic variance. From Fig. 3 these two competing effects cannot be quantified. It should be noted that at least on the largest scale plotted, the contribution of the intrinsic ellipticity distribution to the error (20) is completely negligible compared to the cosmic variance.

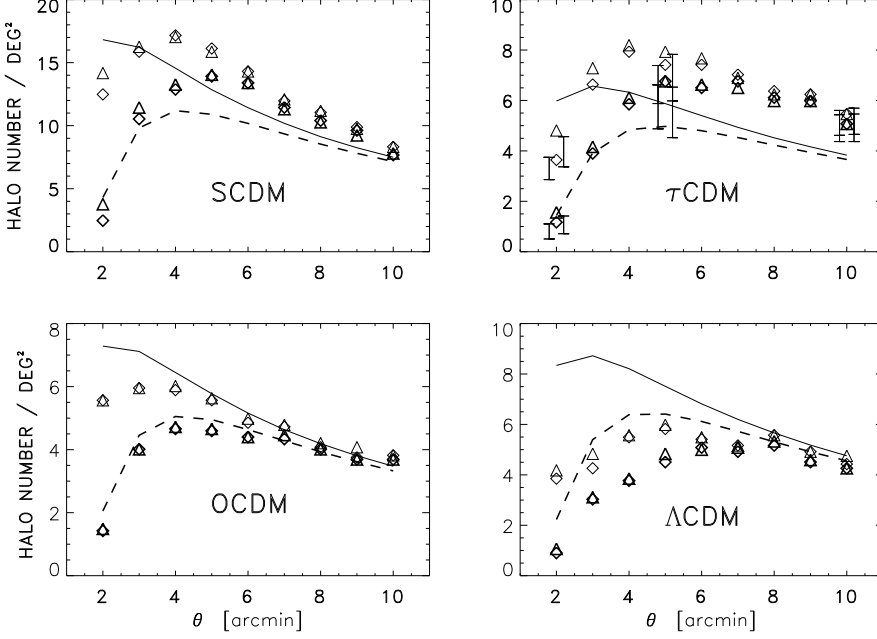


**Fig. 6.** The halo number density  $N(> M_{\text{ap}}, \theta)$  (thin symbols and thin solid curves) and  $N(> M_{\text{ap}}, > 0.6', \theta)$  (thick symbols and thick dashed curves) computed without noise as a function of the filter scale  $\theta$  for four cosmologies as indicated in the panels. Symbols denote results from the simulations ( $\diamond$  from  $\gamma_t$ ,  $\triangle$  from  $g_t$ ) whereas the two line types display the corresponding analytic results from KS1. A signal-to-noise ratio  $S > 5$  is used as detection threshold for the haloes. Error bars in the upper right panel display standard errors from 10 realisations for  $\tau\text{CDM}$  at 2, 5, and 10 arcmin (errors for  $\gamma_t$  offset to the left, errors for  $g_t$  offset to the right)

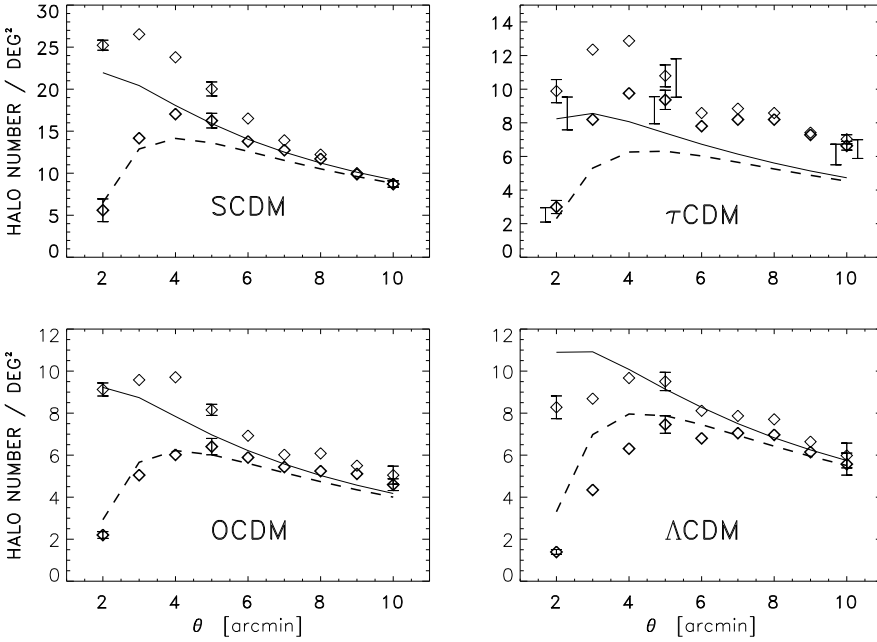


**Fig. 7.** The same as Fig. 6 but with noise from intrinsic ellipticities of the sources added. For the theoretical model this is done by convolving the values from Fig. 6 with a Gaussian, with the dispersion obtained from the intrinsic ellipticity distribution (see KS1). Values from the simulations are denoted by diamonds (thin and thick symbols). Tangential ellipticities now are obtained according to Eq. (10). A signal-to-noise ratio  $S > 5$  is assumed for the haloes. Error bars centred on the halo abundances are standard errors for 7 realisations of the ellipticity distribution at 2, 5, and 10 arcmin. Error bars in the upper right panel for  $\tau\text{CDM}$  are from 10 realisations for 2, 5, and 10 arcmin [error for  $N(> M_5, \theta)$  offset to the right, error for  $N(> M_5, > \zeta_t, \theta)$  offset to the left].

#### 4.2. Halo abundances

As already indicated in Sect. 2.3, high signal-to-noise peaks of  $M_{\text{ap}}$  can be identified with dark matter haloes, rendering the construction of a mass-limited (more correctly: shear-limited) sample feasible. Analytically, the halo abundances can be modelled using the Press & Schechter (1974) prediction for the mass- and redshift-dependent halo number density, and the universal density profile of NFW, while in the simulated  $M_{\text{ap}}$  map all

connected regions above the corresponding threshold are counted as haloes. We shall consider haloes with signal-to-noise ratio  $S$  larger than 5, i.e., a peak in the  $M_{\text{ap}}$  map is counted as a halo if  $M_{\text{ap}} \geq M_5 \equiv 5\sigma_c(\theta)$ .

We consider two differently constructed halo abundances in the following: The first sample is simply  $N(> M_5, \theta)$ , the number density of haloes with an aperture mass larger than  $M_5$  for a given filter size  $\theta$ . The second sample selects peaks with  $M_{\text{ap}} \geq M_5$  within

a connected, cross sectional area of  $\pi\xi_t^2$ , where  $\xi_t$  is the corresponding cross section radius; the number density of such peaks is denoted  $N(> M_5, > \xi_t, \theta)$ . Hence, the size of the peaks in the second sample exceeds the threshold  $\xi_t$ ; these peaks are expected to be more robust with respect to noise coming, e.g., from the intrinsic ellipticity distribution and measurement errors. We use a fixed value of  $\xi_t = 0.6$  arc minutes.

In Fig. 6 the number density of the two halo samples as determined from the simulations without noise are compared to the results from the analytic calculation in KS1 over a range of filter scales  $2' \leq \theta \leq 10'$ . The four panels in Fig. 6 refer to the four cosmological models considered. The error bars for the  $\tau$ CDM model at 2,5, and 10 arcmin are again obtained from the 10 different realisations centred on the arithmetic mean of the realisations.

In general, the number counts determined from simulations agree astonishingly well with the analytical results, considering the simplifying assumptions entering the latter. The deviations between simulations and analytical calculation for three of the four cosmologies, namely SCDM, OCDM, and  $\Lambda$ CDM, and especially for the filter scales above 5 arcmin, are less than 10 %. The largest deviation found for these three models is a factor of 2, for the  $\Lambda$ CDM model at smallest filter scale.

The only notable exception is the  $\tau$ CDM model where the deviation remains above 10 % even for the largest filter scales ( $\theta = 10$  arcmin). This relatively bad agreement has already been noticed for the rms value of  $M_{\text{ap}}$  and is probably due to the fact that the realisation plotted is not characteristic for the mean properties of that model, as also indicated by the fact that the halo abundance lies above the mean of all realisations as indicated by the error bars.

The good agreement between analytic estimates and numerical results for the halo number density are surprising, given that (a) Press-Schechter theory does not exactly reproduce the spatial number density of haloes when compared to N-body simulations, and (b) the universal density profile found by NFW has been obtained by spherical averaging, and therefore cannot account for the non-axisymmetry of their projected density. Furthermore, (c) the haloes found from the simulated  $M_{\text{ap}}$  are expected to be affected by projection effects (Reblinsky & Bartelmann 1999) which are completely neglected in the analytic estimates. Despite these effects which one might suspect to yield significant discrepancies, we find that the analytic estimates are very accurate.

We also investigate the halo abundance in an observationally more realistic situation in Fig. 7, including the noise from the intrinsic ellipticity distribution of the background sources. The plot displays the same quantities as Fig. 6 except for the fact that the halo abundances of the two different samples have been determined using the tangential ellipticities in the case of the simulations.

The analytic estimates are obtained as in KS1. For all four cosmologies, we determined error bars using 7 different realisations of the ellipticity distribution of the background sources (15). The error bars from the 10 realisations shown for  $\tau$ CDM are slightly sub-Poissonian, as in Fig. 6. As expected from the large value of the kurtosis the error coming from the intrinsic ellipticity distribution is much smaller than the error coming from the cosmic variance. On the whole, the number of detected haloes is increased in all cosmologies because, due to the steepness of the Press-Schechter mass function for massive objects, there are more objects just below the threshold than above it. So on average more objects will be lifted above the threshold by noise than brought down below it.

#### 4.3. The tail of $M_{\text{ap}}$

In Fig. 8 we compare the PDF for  $M_{\text{ap}} \geq M_5$  as obtained from analytic calculations (KS2) with that derived from the simulations without noise. The PDF is shown for four filter scales  $\theta = 2, 4, 6, 10$  arcmin in the range  $M_5 \leq M_{\text{ap}} \leq 2M_5$ , for which the analytic results predict a nearly exponential behaviour. Indeed, the numerical PDF in the non-Gaussian tail also seems to follow an exponential rather closely, with a slope very similar to the analytic result.

In order to see how much the PDF varies between different realisations, we have plotted in Fig. 9 the PDF for  $M_5 \leq M_{\text{ap}} \leq 2M_5$  obtained from the 10 realisations in the  $\tau$ CDM model, for 3 filter radii, together with their mean and the corresponding analytic prediction. We find that for the smallest filter scale  $\theta = 2'$ , all 10 realisations are clearly below the analytic result, whereas for the larger filters, the realisation mean of the PDF agrees very well with the analytic prediction.

Remembering that the analytic predictions were made by assuming that all high values of  $M_{\text{ap}}$  are coming from regions close to collapsed haloes, in addition to the assumptions used for estimating the number density of  $M_{\text{ap}}$  peaks (Press-Schechter halo abundance and NFW density profile), this good agreement is somewhat surprising.

## 5. Conclusion

We used ray-tracing simulations through N-body-generated cosmic density distributions to study the statistical properties of the aperture mass  $M_{\text{ap}}$  as a statistics for cosmic shear measurements and for finding dark matter haloes from their shear properties. In particular, we have compared results from these simulations with the available analytic results and found in most cases a very good agreement, except for the skewness which is the least accurate of these predictions. Whereas all other predictions tested here are based on manifestly non-linear

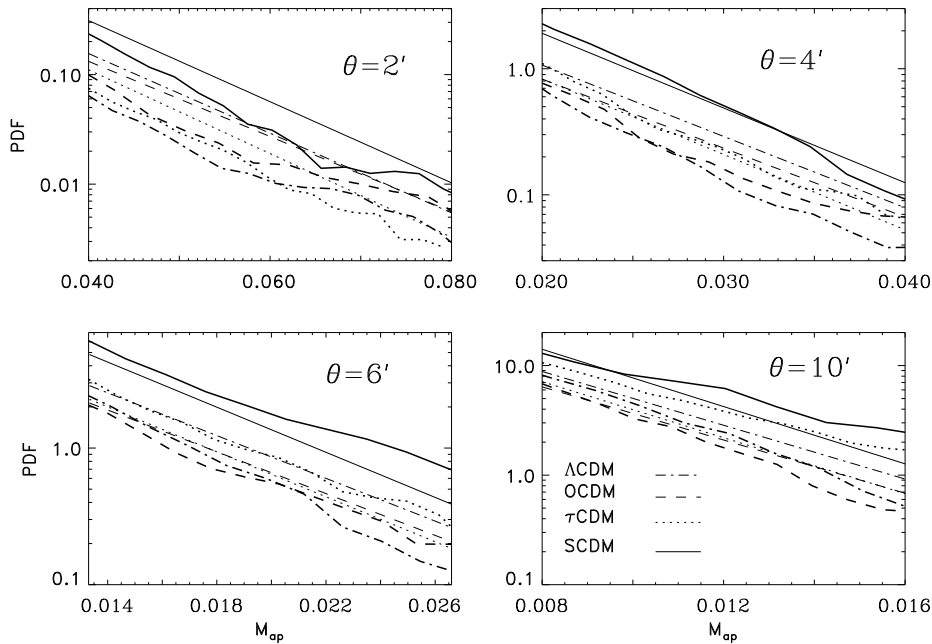


**Fig. 8.** The tail of the PDF of  $M_{\text{ap}}$  for the same cosmologies as indicated in Fig. 2 for different filter scales. In each panel we plot the PDF obtained from the analytic estimate in KS2 with thin lines and that from simulations with thick lines. The line types specifies the cosmology: SCDM (solid line),  $\tau$ CDM (dotted line), OCDM (dashed line) and  $\Lambda$ CDM (dashed-dotted line). The  $M_{\text{ap}}$ -range is  $[M_5, 2M_5]$ , where  $M_5 = S \times 0.016/\theta$  with  $S > 5$  for the parameter specified in the text.

results (like the Press-Schechter halo abundance and the Peacock & Dodds power spectrum), the skewness was estimated analytically by using second-order Eulerian perturbation theory which, on the scales considered, is not very accurate.

Comparing the results from our simulations with analytic studies, we obtain the following main results: (1) The rms of  $M_{\text{ap}}$  is accurately described by analytic results if the fully non-linear prescription of the power spectrum of density fluctuations is used. (2) The statistical error of this rms is dominated by cosmic variance, which in turn depends on the kurtosis of  $M_{\text{ap}}$ . This kurtosis turns out to be relatively large even on angular scales of  $\sim 10'$ , implying the need for many more measurements of  $M_{\text{ap}}$  than expected for a Gaussian field, for a given accuracy of the estimated projected power spectrum. (3) The skewness is only approximately described by analytic considerations based on second-order perturbation theory. (4) The predicted abundance of dark matter haloes detectable at given statistical significance is very well approximated by the semi-analytic theory which combines the Press-Schechter number density of haloes with the universal density profile of Navarro, Frenk & White. (5) Similarly, the functional form of the probability distribution of  $M_{\text{ap}}$  for values much higher than the rms (i.e., in the non-Gaussian tail) is found to closely follow an exponential form, of similar slope and amplitude as predicted by analytic theory which needs to assume that such high values originate due to collapsed haloes. Thus, on the whole, we find that the analytical estimates for the statistical properties of  $M_{\text{ap}}$  are surprisingly accurate.

We also find that our simulations are not sufficiently large for an accurate estimate of the higher-order statistical measures, owing to the finite size of the

simulation box in combination with the large effect of cosmic variance.

As discussed in SvWJK, KS1, KS2, van Waerbeke et al. (1999) and Bartelmann & Schneider (1999), the aperture mass is a useful cosmic shear measure which will eventually allow one to constrain cosmological parameters, completely independent of any assumption on the relation between mass and light. For this purpose, the predictions from cosmology must be known precisely, and our results here indicate that analytic estimates are relatively accurate. Unfortunately, we found a large cosmic variance; e.g., in the estimate of the variance of the rms value of  $M_{\text{ap}}$ , the kurtosis enters and it decreases only rather slowly with increasing filter scale. It can be expected that the first successful application of the aperture mass will be the definition of a sample of haloes defined in terms of their lensing properties only, with a first example given by Erben et al. (1999). The combination of cosmic shear information and CMB measurements can be extremely useful, as shown by Hu & Tegmark (1999), increasing the precision of the determination of cosmological parameters substantially over each of the two individual methods. Their study was based solely on the dispersion of cosmic shear, i.e., on second-order statistics. It is to be expected that a similar combination of CMB results with the PDF of  $M_{\text{ap}}$  will yield even more precise parameter estimates. A detailed study of this combination is expected to be very valuable, but requires a larger grid of cosmological N-body simulations.

*Acknowledgements.* We thank M. Bartelmann for his many valuable suggestions and a careful reading of the manuscript, as well as an anonymous referee for his constructive comments. This work was supported by the ‘‘Sonderforschungsbereich

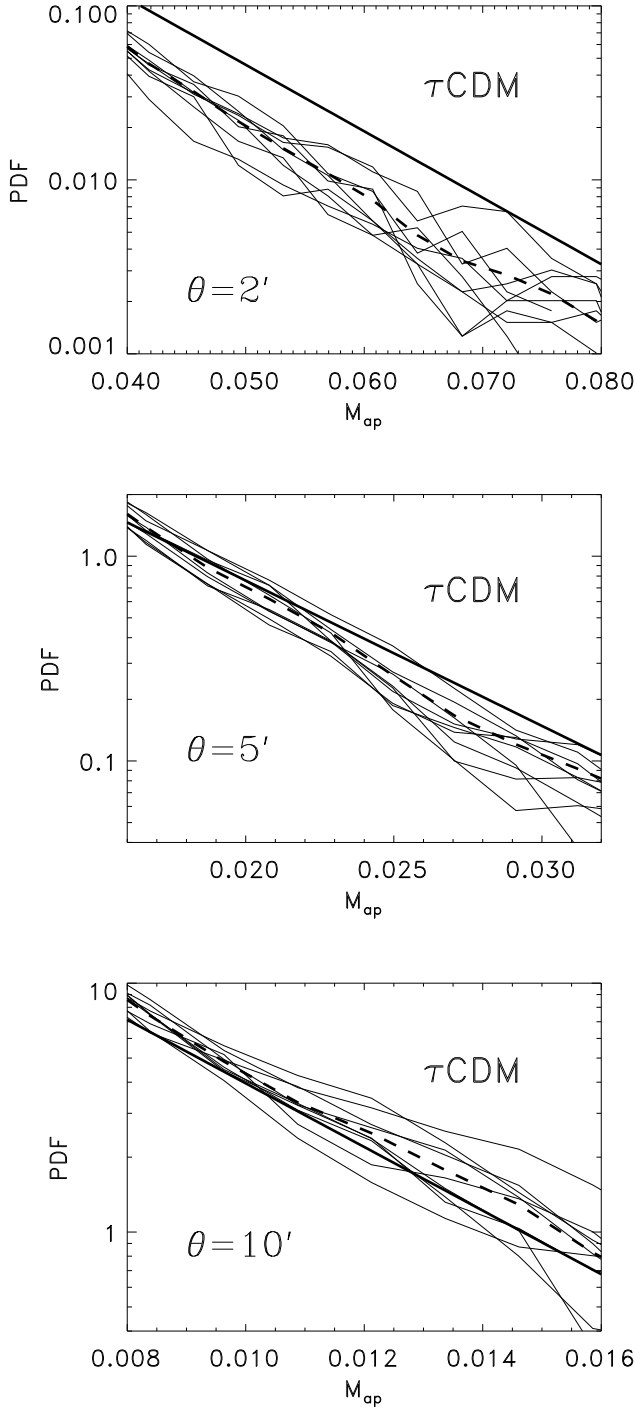


**Fig. 9.** The tail of the PDF of  $M_{\text{ap}}$  for the 10 realisations (thin solid lines) of the  $\tau$ CDM model in comparison to the analytical result (KS2) for the tail of the PDF of  $M_{\text{ap}}$  (thick solid line). In addition, the mean of the 10 realisation (thick dashed line) is plotted. The different panels are for three filter scales, 2, 5, and 10 arcmin.

375-95 für Astro-Teilchenphysik” der Deutschen Forschungsgemeinschaft.

## References

- Bartelmann M., Schneider P., 1999, A&A 345, 17  
 Bartelmann M., Huss A., Colberg J.M., Jenkins A., Pearce F.R., 1998, A&A 330, 1  
 Bernardeau F., 1998, A&A 338, 375  
 Bernardeau F., Van Waerbeke L., Mellier Y., 1997, A&A 322,1  
 Blandford R.D., Saust A.B., Brainerd T.G., Villumsen J.V., 1991, MNRAS 251, 600  
 Couchman H.M.P., Thomas P. A., Pearce F. R., 1995, ApJ 452, 797  
 Diaferio A., Kauffmann G. A., Colberg J.M., White S.D.M., 1999, MNRAS 307, 537  
 Erben T., van Waerbeke L., Mellier Y. et al., 1999, A&A, submitted  
 Fahlman G., Kaiser N., Squires G., Woods D., 1994, ApJ 437, 56  
 Gaztanaga E., Bernardeau F., 1998, A&A 331, 829  
 Hu W., Tegmark M., 1999, ApJ 514, L65  
 Hui L., 1999, ApJ 519L, 9  
 Jain B., Seljak U., 1997, ApJ 484, 560  
 Jain B., Seljak U., White S.D.M., 1999, submitted to ApJ, preprint astro-ph/9901191 (JSW)  
 Jenkins A.R., Frenk C.S., Pearce F.R. et al., 1998, ApJ 499, 20  
 Kaiser N., 1992, ApJ 388, 272  
 Kaiser N., 1998, ApJ 498, 26  
 Kaiser N., Squires G., 1993, ApJ 404, 441  
 Kauffmann G. A., Colberg J.M., Diaferio A., White S.D.M., 1999a, MNRAS 303, 188  
 Kauffmann G. A., Colberg J.M., Diaferio A., White S.D.M., 1999b, MNRAS 307, 529  
 Kruse G., Schneider P., 1999a, MNRAS 302, 821 (KS1)  
 Kruse G., Schneider P., 1999b, submitted to MNRAS, preprint astro-ph/9904192 (KS2)  
 Lombardi M., Bertin G., 1998a, A&A 330, 791  
 Lombardi M., Bertin G., 1998b, A&A 335, 1  
 Miralda-Escude J., 1991, ApJ 380, 1  
 Navarro J.F., Frenk C.S., White S.D.M., 1996, ApJ 462 563 (NFW)  
 Navarro J.F., Frenk C.S., White S.D.M., 1997, ApJ 490, 493 (NFW)  
 Peacock J.A., Dodds S.J., 1996, MNRAS 280, L19  
 Pearce F.R., Couchman H.M.P., 1997, NewA 2, 411  
 Press W.H., Schechter P. 1974, ApJ 187, 425  
 Reblinsky K., Bartelmann M., 1999, A&A 345,1  
 Schneider P., 1995, A&A 302, 639  
 Schneider P. 1996, MNRAS 283, 837 (S96)  
 Schneider P., Weiss A., 1988, ApJ 330, 1  
 Schneider. P., Ehlers J., Falco E. E., 1992, *Gravitational Lenses*, Springer Verlag, Berlin  
 Schneider P., van Waerbeke L., Jain B., Kruse G. 1998, MNRAS 296, 873 (SvWJK)  
 Schramm T., Kayser R., 1995, A&A 299, 1  
 Scoccimarro R., Frieman J., 1999, ApJ 520, 35  
 Seitz C., Schneider P., 1997, A&A 318, 687  
 Seitz S., Schneider P., 1996, A&A 305, 383  
 Seitz S., Schneider P., Ehlers J., 1994, Class. Quant. Grav. 11, 2345  
 Seitz S., Schneider P., Bartelmann M., 1998a, A&A 337, 325

- Seitz S., Saglia R.P., Bender R., Hopp U., Belloni P., Ziegler B., 1998b, MNRAS 298, 945
- Tyson J.A., Valdes F., Wenk R.A., 1990, ApJ 349, L1
- van Waerbeke L., Bernardeau F., Mellier Y., 1999, A&A 342,15